

ICMM2005-75109

PRESSURE DROP OF FULLY-DEVELOPED, LAMINAR FLOW IN MICROCHANNELS OF ARBITRARY CROSS-SECTION

M. Bahrami¹, M. M. Yovanovich², and J. R. Culham³
Microelectronics Heat Transfer Laboratory
Department of Mechanical Engineering
University of Waterloo, Waterloo, ON, Canada N2L 3G1

Abstract

Pressure drop of fully developed, laminar, incompressible flow in smooth mini and microchannels of arbitrary cross-section is investigated. A compact approximate model is proposed that predicts the pressure drop for a wide variety of shapes. The model is only a function of geometrical parameters of the cross-section, i.e., area, perimeter, and polar moment of inertia. The proposed model is compared with analytical and numerical solutions for several shapes. Also, the comparison of the model with experimental data, collected by several researchers, shows good agreement.

Nomenclature

A	=	cross-sectional area, m^2
b, c	=	channel semi-axes, m
D_h	=	hydraulic diameter $4A/P$, m
$E(\cdot)$	=	complete elliptic integral of the second kind
f	=	Fanning friction factor, $2\tau/\rho\bar{w}^2$
h	=	height of trapezoidal channel, m
I_p	=	polar moment of inertia, m^4
I_p^*	=	specific polar moment of inertia, I_p/A^2
L	=	microtube length, m
n	=	number of sides, regular polygons
P	=	perimeter, m
$Re_{\sqrt{A}}$	=	Reynolds number, $\rho\bar{w}\sqrt{A}/\mu$
w	=	fluid velocity, m/s
\bar{w}	=	mean fluid velocity, m/s
z	=	flow direction

Greek

α^*	=	aspect ratio trapezoidal duct, h/a
β	=	dimensionless parameter trapezoidal duct
ϵ	=	aspect ratio, c/b
ρ	=	fluid density, kg/m^3
μ	=	fluid viscosity, $kg/m.s$
τ	=	wall shear stress, N/m^2
$\bar{\tau}^*$	=	non-dimensional wall shear stress, $[-]$
ϕ	=	trapezoidal channel angle, rad
Δp	=	pressure drop, Pa
Γ	=	boundary of duct

Subscripts

\sqrt{A}	=	square root of cross-sectional area, m
------------	---	--

1 INTRODUCTION

Advances in microfabrication make it possible to build microchannels with small characteristic lengths, in the order of micrometers. Micro and minichannels show promising potential for being incorporated in a wide variety of unique, compact, and efficient cooling applications such as in microelectronic devices. These micro heat exchangers or heat sinks feature extremely high heat transfer surface area per unit volume ratios, high heat transfer coefficients, and low thermal resistances [1]. Microchannels can be produced directly by techniques such as chemical etching on silicon wafers. As a result, the cross-section of the channels depends on a variety of factors, such as the crystallographic nature of the silicon used. According to Morini [2], when a KOH-anisotropic etching technique is employed, it is possible to obtain microchannels which have a fixed cross-section. Shape of the cross-section depends on the

¹Post-Doctoral Fellow. Mem. ASME. Corresponding author. E-mail: majid@mhtlab.uwaterloo.ca.

²Distinguished Professor Emeritus. Fellow ASME.

³Associate Professor and Director of MHTL. Mem. ASME.

orientation of the silicon crystal planes. For instance, the microchannels etched in 100 or in 110 silicon will have a trapezoidal cross-section with an apex angle of 54.7° imposed by the crystallographic morphology of the silicon or a rectangular cross-section, respectively [2].

Tuckerman and Pease [3] were the first to demonstrate that planar integrated circuit chips can be effectively cooled by laminar water flowing through microchannels with hydraulic diameters of 86 to 95 μm . However, due to small scale channel sizes, the pressure drop and the required pumping power dramatically increase. Therefore simultaneous hydrodynamic and thermal analyses must be performed to investigate the effects of both flow and heat transfer in micro or minichannels.

In recent years, a large number of papers have reported pressure drop data for laminar flow of liquids in microchannels with various cross-sections. However, published results are often inconsistent. According to [4], some of these authors conducted experiments in non-circular microchannels, but compared their pressure drop data with the classical values of $fRe=16$ or 64 of circular pipes. Some of the discrepancies in the published data can be explained within the limits of continuum fluid mechanics; Bahrami et al. [5] developed a model that captures the observed trends in *rough* microchannels. Recently, Liu and Garimella [6] and Wu and Cheng [7] conducted experiments in *smooth* rectangular and trapezoidal microchannels, respectively; they reported that the Navier-Stokes equations are valid for laminar flow in smooth microchannels.

In the literature there are no comprehensive and encompassing models or correlations that predict pressure drop in arbitrary cross-sections. Thus the objective of this work is to develop a compact approximate model that provides the pressure drop in micro and minichannels of arbitrary cross-section. The model estimates the pressure drop (within 8% accuracy) and provides tools for basic design, parametric studies, and optimization analyses required for microchannel heat exchangers and heat sinks.

2 PROBLEM STATEMENT

Consider fully developed, steady-state laminar flow in a two dimensional channel with the boundary Γ , constant cross-sectional area A , and constant perimeter P as shown in Fig. 1. The flow is assumed to be incompressible and have constant properties. Moreover, body forces such as gravity, centrifugal, Coriolis, and electromagnetic do not exist. Also, the rarefaction and surface effects are assumed to be negligible and the fluid is considered to be a continuum. For such a flow, the Navier-Stokes equations reduce to the momentum equation which is also known as *Poisson's equation*. In this case, the source term in Poisson's

equation is the constant pressure gradient along the length of the duct, $\Delta p/L$. The governing equation for fully developed laminar flow in a constant cross-sectional area channel is [8]:

$$\nabla^2 w = \frac{1}{\mu} \frac{dp}{dz} \quad \text{with} \quad w = 0 \text{ on } \Gamma \quad (1)$$

where w and z are the fluid velocity and the flow direction, respectively. The boundary condition for the velocity is the no-slip condition at the wall.

The velocity profile is constant in the longitudinal direction; thus the pressure gradient applied at the ends of the channel must be balanced by the shear stress on the wall of the channel

$$\bar{\tau}PL = \Delta p A \quad (2)$$

where

$$\bar{\tau} = \frac{1}{A} \int_{\Gamma} \tau dA$$

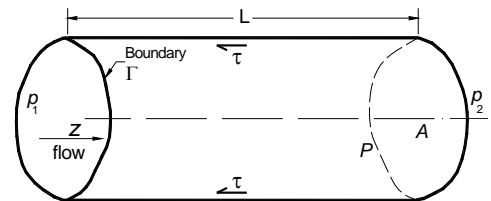


Figure 1. MICROCHANNEL OF ARBITRARY CONSTANT CROSS-SECTION, $L \gg \sqrt{A}$

3 EXACT SOLUTIONS

In this section, relationships are derived for pressure drop and the product of Reynolds number and Fanning friction factor, fRe , of fully developed laminar flow for some cross-sections using existing analytical solutions. The analytical solutions for the relevant flow fields can be found in fluid mechanics textbooks such as White [9] and [10]. The proceeding method, described for the elliptical microchannels, can be applied for other shapes listed in Table 1. Therefore, it is left to the reader to follow the steps for other cross-sections.

The governing equation is the Poisson's equation, Eq. (1). An analytical solution exists for the laminar fluid flow in elliptical microchannels with the following *mean velocity*

$$\bar{w} = \frac{b^2 c^2}{4(b^2 + c^2)} \frac{\Delta p}{\mu L} \quad (3)$$

where b and c are the major and minor semi-axes of the cross-section, $b \geq c$. An aspect ratio is defined for the elliptical microchannel

$$0 < \epsilon \equiv \frac{c}{b} \leq 1 \quad (4)$$

For an elliptical microchannel, the cross-sectional area and the perimeter are

$$\begin{cases} A = \pi bc \\ P = 4b E(\sqrt{1 - \epsilon^2}) \end{cases} \quad (5)$$

where $E(\cdot)$ ⁴ is the complete elliptic integral of the second kind. The mean velocity can be presented in terms of the aspect ratio, ϵ ,

$$\bar{w} = \frac{c^2}{4(1 + \epsilon^2)} \frac{\Delta p}{\mu L} \quad (6)$$

which can be re-arranged as

$$\frac{\Delta p}{L} = \frac{4(1 + \epsilon^2)}{c^2} \mu \bar{w} \quad (7)$$

Combining Eqs. (2) and (7), the mean wall shear stress is

$$\bar{\tau} = \frac{4\mu(1 + \epsilon^2)\bar{w}A}{c^2 P} \quad (8)$$

The ratio of the cross-sectional area over perimeter for elliptical microchannels is

$$\frac{A}{P} = \frac{\pi c}{4E(\sqrt{1 - \epsilon^2})} \quad (9)$$

The mean wall shear stress becomes

$$\bar{\tau} = \frac{\pi\mu(1 + \epsilon^2)\bar{w}}{cE(\sqrt{1 - \epsilon^2})} \quad (10)$$

A relationship can be found between the minor axis c and the area, Eq. (5),

$$c = \sqrt{\frac{A\epsilon}{\pi}} \quad (11)$$

Substituting Eq. (11) in Eq. (10), one finds

$$\bar{\tau} = \frac{\pi\sqrt{\pi}(1 + \epsilon^2)}{\sqrt{\epsilon}E(\sqrt{1 - \epsilon^2})} \frac{\mu\bar{w}}{\sqrt{A}} \quad (12)$$

It is conventional to use the ratio of area over perimeter $D_h = 4A/P$, known as the *hydraulic diameter*, as the characteristic length scale for non-circular channels. However, as can be seen in Eq. (12), a more appropriate length scale is

the *square root of area*, \sqrt{A} . Muzychka and Yovanovich [11] showed that the apparent friction factor is a weak function of the shape of the geometry of the channel by defining aspect ratios for various cross-sections. Later, it will be shown that the selection of the square root of area as the characteristic length leads to similar trends in $fRe_{\sqrt{A}}$ for elliptical and rectangular channels with identical cross-sectional area.

With the square root of area \sqrt{A} as the characteristic length scale, a non-dimensional wall shear stress can be defined as:

$$\bar{\tau}^* \equiv \frac{\bar{\tau}\sqrt{A}}{\mu\bar{w}} = \frac{\pi\sqrt{\pi}(1 + \epsilon^2)}{\sqrt{\epsilon}E(\sqrt{1 - \epsilon^2})} \quad (13)$$

It should be noted that the right hand side of Eq. (13) is only a function of the aspect ratio (geometry) of the channel.

The Fanning friction factor is defined as

$$f \equiv \frac{\bar{\tau}}{\frac{1}{2}\rho\bar{w}^2} \quad (14)$$

Using Eq. (12), the Fanning friction factor of elliptical microchannels becomes

$$f = \frac{2\pi\sqrt{\pi}(1 + \epsilon^2)}{\sqrt{\epsilon}E(\sqrt{1 - \epsilon^2})} \frac{\mu}{\rho\bar{w}\sqrt{A}} \quad (15)$$

Reynolds number can be defined based on the square root of area \sqrt{A}

$$Re_{\sqrt{A}} = \frac{\rho\bar{w}\sqrt{A}}{\mu} \quad (16)$$

Equation (15) becomes

$$fRe_{\sqrt{A}} = \frac{2\pi\sqrt{\pi}(1 + \epsilon^2)}{\sqrt{\epsilon}E(\sqrt{1 - \epsilon^2})} \quad (17)$$

Similar to $\bar{\tau}^*$, $fRe_{\sqrt{A}}$ is only a function of the geometry of the channel. Thus, a relationship can be found between the non-dimensional friction factor $\bar{\tau}^*$ and $fRe_{\sqrt{A}}$

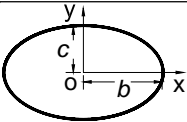
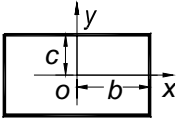
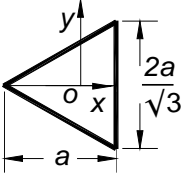
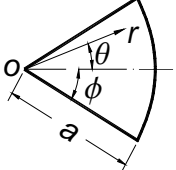
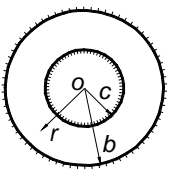
$$fRe_{\sqrt{A}} = 2\bar{\tau}^* \quad (18)$$

Following the same steps described above, relationships for $fRe_{\sqrt{A}}$ are determined for other microchannel cross-sections and they are summarized in Table 1. With respect to Table 1, the following should be noted:

1) the original analytical solution for the mean velocity in rectangular channels is in the form of a series. However, when $\epsilon = 1$ (square), the first term of the series gives the value $fRe_{\sqrt{A}} = 14.132$ compared with the exact value (full

⁴ $E(x) = \int_0^{\pi/2} \sqrt{1 - x^2 \sin^2 t} dt$

Table 1. ANALYTICAL SOLUTIONS OF fRe FOR VARIOUS CROSS-SECTIONS

cross-section	Area, Perimeter	mean velocity (analytical) \bar{w} [9; 10]	$fRe_{\sqrt{A}}$
	$A = \pi bc$ $P = 4bE(\sqrt{1-\epsilon^2})$	$\frac{c^2}{4(1+\epsilon^2)} \frac{\Delta p}{\mu L}$	$\frac{2\pi\sqrt{\pi}(1+\epsilon^2)}{\sqrt{\epsilon}E(\sqrt{1-\epsilon^2})}$
	$A = 4bc$ $P = 4(b+c)$	$\frac{\Delta p c^2}{\mu L} \left[\frac{1}{3} - \frac{64c}{\pi^5 b} \tanh\left(\frac{\pi b}{2c}\right) \right]$	$\frac{12}{\left[1 - \frac{192}{\pi^5} \epsilon \tanh\left(\frac{\pi}{2\epsilon}\right) \right]} (1+\epsilon) \sqrt{\epsilon}$
	$A = a^2/\sqrt{3}$ $P = 6a/\sqrt{3}$	$\frac{1}{60} \frac{\Delta p a^2}{\mu L}$	$\frac{20}{3^{1/4}} = 15.197$
	$A = \phi a^2$ $P = 2a(1+\phi)$	$\frac{\Delta p a^2}{\mu L} g(\phi)^{[1]}$	$\frac{\phi\sqrt{\phi}}{(1+\phi)g(\phi)^{[1]}}$
	$A = \pi(b^2 - c^2)$ $P = 2\pi(b+c)$	$\frac{\Delta p b^2}{8\mu L} \left(\epsilon^2 - 1 + \frac{2\ln(1/\epsilon) + \epsilon^2 - 1}{\ln(1/\epsilon)} \right)$	$\frac{8\sqrt{\pi}(1-\epsilon)\sqrt{1-\epsilon^2}}{\left(\epsilon^2 - 1 + \frac{2\ln(1/\epsilon) + \epsilon^2 - 1}{\ln(1/\epsilon)} \right)}$
${}^1g(\phi) = \frac{\tan(2\phi) - 2\phi}{16\phi} - \frac{128\phi^3}{\pi^5} \sum_{n=1}^{\infty} \left[\frac{1}{(2n-1)^2(2n-1+4\phi/\pi)^2(2n-1-4\phi/\pi)} \right]$		$\epsilon = c/b$	

series solution) of 14.23. The maximum difference of approximately 0.7% occurs at $\epsilon = 1$. For smaller values of ϵ , the agreement with the full series solution is even better. Therefore, only the first term is employed in this study.

2) for rectangular microchannels, two asymptotes can be recognized, i.e., the very narrow rectangular and square channels [12]

$$\begin{aligned}
 fRe_{\sqrt{A}} &= \frac{12}{\sqrt{\epsilon}} & \epsilon \rightarrow 0 \\
 fRe_{\sqrt{A}} &= 14.132 & \epsilon = 1
 \end{aligned} \tag{19}$$

3) for elliptical microchannels, the asymptotes are the very narrow elliptical and circular microchannels [12]

$$\begin{aligned}
 fRe_{\sqrt{A}} &= \frac{11.15}{\sqrt{\epsilon}} & \epsilon \rightarrow 0 \\
 fRe_{\sqrt{A}} &= 14.179 & \epsilon = 1
 \end{aligned} \tag{20}$$

Note that the $fRe_{\sqrt{A}}$ values and trends for elliptical and rectangular channels are very close at both asymptotes. Figure 2 shows the comparison between $fRe_{\sqrt{A}}$ relationships for the rectangular and elliptical microchannels reported in Table 1. In spite of the different forms of the

$fRe_{\sqrt{A}}$ for rectangular and elliptical microchannels, trends of both formulae are very similar as the aspect ratio varies between $0 < \epsilon \leq 1$. The maximum relative difference is less than 8%.

Elliptical and rectangular cross-sections cover a wide range of singly-connected microchannels. With the similarity in the trends of solutions for these cross-sections, one can conclude that a general, *purely geometrical*, relationship may exist that predicts $fRe_{\sqrt{A}}$ for arbitrary singly-connected cross-sections. Based on this observation, an *approximate model* is developed in the next section.

4 APPROXIMATE SOLUTION

Exact relationships for $fRe_{\sqrt{A}}$ are reported for the elliptical, rectangular, and some other shapes in the previous section. However, finding exact solutions for many practical singly-connected cross-sections, such as trapezoidal microchannels, is complex and/or impossible. In many practical instances such as basic design, parametric study, and optimization analyses, it is often required to obtain the trends and a reasonable estimate of the pressure drop. Moreover, as a result of recent advances in fabrication technologies in MEMS and microfluidic devices, cross-sections such as trapezoidal have become more important. Therefore, an approximate compact model that estimates pressure drop of arbitrary cross-sections will be of great value.

Torsion in beams and fully developed laminar flow in ducts are similar because the governing equation for both problems is Poisson's equation, Eq. (1). Comparing various singly connected cross-sections, Saint-Venant (1880) found that the torsional rigidity of a shaft could be accurately approximated by using an equivalent elliptical cross-section, where both cross-sectional area and *polar moment of inertia* are maintained the same as the original shaft [13]. With a similar approach as Saint-Venant, a model will be developed for predicting pressure drop in channels of arbitrary cross-section based on the solution for an elliptical duct.

The elliptical channel is considered, not because it is likely to occur in practice, but rather to utilize the unique geometrical property of its velocity solution. The mean velocity of elliptical channels is known, Eq. (3). The polar moment of inertia, I_p^5 , for an ellipse is

$$I_p = \frac{\pi bc(b^2 + c^2)}{4} \quad (21)$$

Equation (7) can be re-arranged in terms of the polar moment of inertia, about its center, as follows:

$$\frac{\Delta p}{L} = \frac{16\pi^2 \mu \bar{w}}{A^3} I_p = \frac{16\pi^2 \mu \bar{w}}{A} I_p^* \quad (22)$$

⁵ $I_p = \int (x^2 + y^2) dA$, where x and y are distances from x and y axes.

where $I_p^* = I_p/A^2$ is a non-dimensional geometrical parameter which we call the *specific polar moment of inertia*. Combining Eqs. (2) and (22), one can write

$$\bar{\tau} = \frac{16\pi^2 \mu \bar{w}}{\sqrt{A}} \frac{\sqrt{A}}{P} I_p^* \quad (23)$$

Note that \sqrt{A}/P is also a non-dimensional parameter. Using Eq. (23), the Fanning friction factor, Eq. (14), can be determined

$$f = 32\pi^2 \underbrace{\frac{\mu}{\rho \bar{w} \sqrt{A}}}_{1/Re_{\sqrt{A}}} \frac{\sqrt{A}}{P} I_p^* \quad (24)$$

or

$$fRe_{\sqrt{A}} = 32\pi^2 I_p^* \frac{\sqrt{A}}{P} \quad (25)$$

Using Eq. (18), one can find the non-dimensional shear stress

$$\bar{\tau}^* = \frac{1}{2} fRe_{\sqrt{A}} = 16\pi^2 I_p^* \frac{\sqrt{A}}{P} \quad (26)$$

The right hand side of Eqs. (25) and (26) are general geometrical functions since I_p , A , and P are general geometrical parameters. Therefore the approximate model assumes that for constant fluid properties and flow rate in a constant cross-section channel, $\bar{\tau}^*$ and $fRe_{\sqrt{A}}$ are only functions of the non-dimensional geometric parameter, $I_p^* \sqrt{A}/P$, of the cross-section.

Employing Eq. (25), one only needs to compute the non-dimensional parameter $I_p^* \sqrt{A}/P$ of the channel to determine the $fRe_{\sqrt{A}}$ value. On the other hand, using the conventional method, Poisson's equation must be solved to find the velocity field and the mean velocity; then the procedure described in the previous section should be followed to find $fRe_{\sqrt{A}}$. This clearly shows the convenience of the approximate model.

To validate the approximate model, the exact values of $fRe_{\sqrt{A}}$ for some cross-sections are compared with the approximate model, i.e., Eq. (25), in Table 2 (in Appendix). Also the geometric parameter $I_p^* \sqrt{A}/P$ is reported for a variety of cross-sections in Table 2. The approximate model shows relatively good agreement, within 8% relative difference, with the exact solutions for the cross-sections considered, except for the equilateral triangular channel. Moreover, the non-dimensional geometric parameter is derived for regular polygons and trapezoidal channels; the approximate model is compared with the numerical values for these shapes published by Shah and London [8].

4.1 Regular Polygons

Figure 3 illustrates a regular polygon microchannel of the side length a . For regular polygons, cross-sectional area,

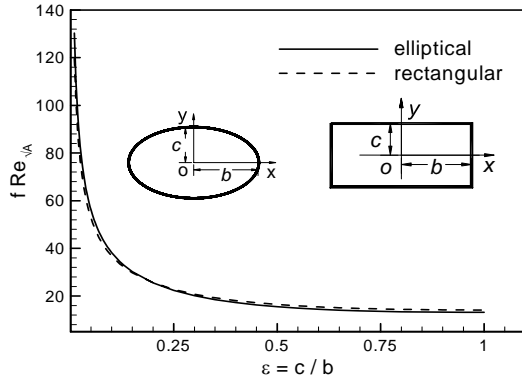


Figure 2. COMPARISON OF $f Re_{\sqrt{A}}$ FOR ELLIPTICAL AND RECTANGULAR MICROCHANNELS

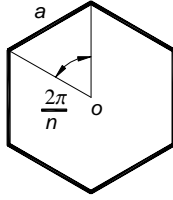


Figure 3. CROSS-SECTION OF A REGULAR POLYGON CHANNEL

perimeter, and the polar moment of inertia are

$$A = \frac{na^2}{4 \tan\left(\frac{\pi}{n}\right)} \quad (27)$$

$$P = na \quad (28)$$

$$I_p = \frac{na^4}{96 \tan\left(\frac{\pi}{n}\right)} \left[1 + \frac{3}{\tan^2\left(\frac{\pi}{n}\right)} \right] \quad (29)$$

Therefore,

$$I_p^* = \frac{I_p}{A^2} = \frac{\tan\left(\frac{\pi}{n}\right)}{6n} \left[1 + \frac{3}{\tan^2\left(\frac{\pi}{n}\right)} \right] \quad (30)$$

$$\frac{\sqrt{A}}{P} = \frac{1}{2\sqrt{n \tan\left(\frac{\pi}{n}\right)}} \quad (31)$$

Finally, one can obtain $f Re_{\sqrt{A}}$

$$f Re_{\sqrt{A}} = \frac{8\pi^2 \tan\left(\frac{\pi}{n}\right)}{3n\sqrt{n \tan\left(\frac{\pi}{n}\right)}} \left[1 + \frac{3}{\tan^2\left(\frac{\pi}{n}\right)} \right] \quad (32)$$

Table 3. GEOMETRIC PARAMETER FOR REGULAR POLYGONS

n	I_p^*	\sqrt{A}/P	$f Re_{\sqrt{A}}$	
			model	numerical [8]
3	0.19245	0.2193	13.328	15.196
4	0.16666	0.2500	13.138	14.227
5	0.16181	0.2623	13.391	14.044
6	0.16037	0.2686	13.612	14.009
7	0.15979	0.2723	13.830	14.055
10	0.15929	0.2773	13.960	14.060
∞	0.15915	0.2821	14.181	14.180

Table 3 lists the geometric parameter I_p^* , \sqrt{A}/P , and $f Re_{\sqrt{A}}$ for regular polygons. Table 3 also shows the comparison between the approximate model with the numerical results reported for regular polygons by Shah and London [8]. The following relationship is used to convert the Reynolds number Fanning friction factor product based on D_h to \sqrt{A}

$$f Re_{\sqrt{A}} = \frac{P}{4\sqrt{A}} f Re_{D_h} \quad (33)$$

The approximate model shows good agreement, within 8% relative difference, with the numerical results of [8] except for the equilateral triangular ($n = 3$); the agreement improves as the number of sides increases toward the circular channel ($n \rightarrow \infty$). Using a *mapping* approach, a compact model is developed in Appendix A which predicts the $f Re_{\sqrt{A}}$ for isosceles triangular channels with a maximum difference less than 3.5%.

4.2 Trapezoidal Microchannel

The cross-section of a trapezoidal microchannel is shown in Fig. 4. This is an important shape since some microchannels are manufactured with trapezoidal cross-sections as a result of the etching process in silicon wafers. Furthermore, in the limit when the top side length, a , goes to zero; it yields an isosceles triangle. At the other limit when $a = b$, it yields rectangular; and a square microchannel when $a = b = h$. The cross-sectional area, perimeter, and polar moment of inertia (about its center) are

$$A = \frac{h}{2} (a + b) \quad (34)$$

$$P = a + b + 2c \quad (35)$$

$$I_p = \frac{h}{144(a+b)} \left\{ (a^2 + b^2) [3(a+b)^2 + 4h^2] + 16h^2 ab \right\} \quad (36)$$

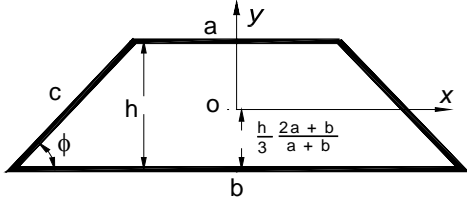


Figure 4. CROSS-SECTION OF AN ISOSCELES TRAPZOIDAL CHANNEL

Table 4. LIMITING CASES OF ISOSCELES TRAPEZOID

cross-section	ϵ	β	I_p^*	\sqrt{A}/P
triangular ¹	$\frac{b}{2h}$	0	$\frac{3\epsilon^2 + 1}{18\epsilon}$	$\frac{\sqrt{\epsilon}}{2(\epsilon + \sqrt{\epsilon^2 + 1})}$
triangular ²	$\frac{1}{\sqrt{3}}$	0	$\frac{\sqrt{3}}{9}$	$\frac{\sqrt{3}}{6(3)^{1/4}}$
rectangular	$\frac{b}{h}$	1	$\frac{1 + \epsilon^2}{12\epsilon}$	$\frac{\sqrt{3}}{2(1 + \epsilon)}$
square	1	1	$\frac{1}{6}$	$\frac{1}{4}$
¹ isosceles	² equilateral			

An aspect ratio is defined

$$\epsilon \equiv \frac{a+b}{2h} \quad (37)$$

The aspect ratio should work for all above-mentioned limiting cases. As shown in Table 4, the defined aspect ratio covers the triangular, rectangular, and square limiting cases. The polar moment of inertia can be re-arranged and presented as

$$I_p = \frac{A^2 [2(3\epsilon^2 + 1) + \beta(1 - 3\epsilon^2)]}{36\epsilon} \quad (38)$$

where β , another non-dimensional parameter, is defined as

$$\beta \equiv \frac{h^2 ab}{A^2} = \frac{4ab}{(a+b)^2} \quad (39)$$

Note that the parameter β is zero for triangular and 1 for rectangular and square channels. The angle ϕ , see Fig. 4, can be found from ϵ and β

$$\sin \phi = \frac{1}{\sqrt{\epsilon^2 - \beta\epsilon^2 + 1}} \quad (40)$$

The specific polar moment of inertia is

$$I_p^* = \frac{I_p}{A^2} = \frac{2(3\epsilon^2 + 1) + \beta(1 - 3\epsilon^2)}{36\epsilon} \quad (41)$$

The perimeter, Eq. (35), in terms of non-dimensional geometrical parameters is

$$P = 2h \left(\epsilon + \sqrt{\epsilon^2 - \beta\epsilon^2 + 1} \right) \quad (42)$$

From the cross-sectional area, Eq. (34), one can obtain, $A = \epsilon h^2$; thus, one can write:

$$\frac{\sqrt{A}}{P} = \frac{\sqrt{\epsilon}}{2 \left(\epsilon + \sqrt{\epsilon^2 - \beta\epsilon^2 + 1} \right)} \quad (43)$$

$$fRe_{\sqrt{A}} = \frac{8\pi^2 (3\epsilon^2 + 1) + \beta(1 - 3\epsilon^2)}{9\sqrt{\epsilon} \left(\epsilon + \sqrt{\epsilon^2 - \beta\epsilon^2 + 1} \right)} \quad (44)$$

Shah and London [8] reported numerical values for fRe_{D_h} for laminar fully developed flow in trapezoidal channel. They presented fRe_{D_h} values as a function of $\alpha^* = h/a$ for different values of angles ϕ . The non-dimensional geometrical parameters ϵ and β , defined in this work, are related to α^* and ϕ as follows:

$$\begin{aligned} \epsilon &= \frac{1}{\alpha^*} + \frac{1}{\tan \phi} \\ \beta &= 1 - \frac{1}{\epsilon^2 \tan^2 \phi} \end{aligned} \quad (45)$$

Table 5 shows the comparison between the approximate model and the numerical data reported by [8]. As can be seen, except for a few points, the agreement between the approximate model and the numerical values is reasonable (less than 10%).

5 COMPARISON WITH EXPERIMENTAL DATA

The present model is compared with experimental data collected by several researchers [7; 6; 14] for microchannels. The accuracy of the experimental data is in the order of 10%.

Wu and Cheng [7] conducted experiments and measured the friction factor of laminar flow of deionized water in smooth silicon microchannels of trapezoidal cross-sections. Table 6 summarizes geometric parameters of their microchannels.

Figures 5 and 6 are examples of the comparison between the approximate model and the data of [7] for channels N1-100 and N2-200, respectively. As shown the approximate model shows good agreement with these data.

The frictional resistance $fRe_{\sqrt{A}}$ is not a function of Re number, i.e., it remains constant for the laminar regime as the Reynolds number varies. Therefore, the experimental data for each set are averaged over the laminar region. As a result, for each experimental data set, one ϵ , one β , and

Table 5. MODEL VS DATA [8], TRAPEZOIDAL CHANNELS

α^*	fRe_{D_h}	ϵ	β	$fRe_{\sqrt{A}}^b$		
				model	[8]	%dif.
$\phi=85^\circ$						
8	17.474	0.212	0.830	23.384	23.054	1.41
4	16.740	0.337	0.933	18.563	19.325	-4.11
2	15.015	0.587	0.978	14.516	15.587	-7.38
4/3	14.312	0.837	0.989	13.318	14.398	-8.11
1	14.235	1.087	0.994	13.203	14.274	-8.11
3/4	14.576	1.421	0.996	13.774	14.825	-7.63
1/2	15.676	2.087	0.998	15.806	16.770	-6.10
1/4	18.297	4.087	1.000	22.648	23.038	-1.72
1/8	20.599	8.087	1.000	33.804	32.926	2.60
$\phi=75^\circ$						
8	14.907	0.393	0.535	15.745	16.982	-7.85
4	14.959	0.518	0.732	14.725	16.142	-9.62
2	14.340	0.768	0.878	13.499	14.754	-9.30
4/3	14.118	1.018	0.931	13.244	14.365	-8.46
1	14.252	1.268	0.955	13.520	14.576	-7.81
3/4	14.697	1.601	0.972	14.304	15.311	-7.04
1/2	15.804	2.268	0.986	16.430	17.332	-5.49
1/4	18.313	4.268	0.996	23.165	23.505	-1.47
1/8	20.556	8.268	0.999	34.155	33.254	2.64
$\phi=60^\circ$						
8	13.867	0.702	0.324	13.540	15.364	-13.47
4	13.916	0.827	0.513	13.544	15.162	-11.95
2	13.804	1.077	0.713	13.623	14.842	-8.95
4/3	13.888	1.327	0.811	13.953	14.960	-7.21
1	14.151	1.577	0.866	14.484	15.392	-6.26
3/4	14.637	1.911	0.909	15.384	16.230	-5.49
1/2	15.693	2.577	0.950	17.482	18.241	-4.34
1/4	18.053	4.577	0.984	23.908	24.184	-1.15
1/8	20.304	8.577	0.995	34.582	33.735	2.45
$\phi=45^\circ$						
8	13.301	1.125	0.210	14.669	15.921	-8.53
4	13.323	1.250	0.360	14.796	15.874	-7.28
2	13.364	1.500	0.556	15.123	15.899	-5.13
4/3	13.541	1.750	0.673	15.573	16.194	-3.99
1	13.827	2.000	0.750	16.125	16.691	-3.51
3/4	14.260	2.333	0.816	16.973	17.492	-3.06
1/2	15.206	3.000	0.889	18.869	19.377	-2.69
1/4	17.397	5.000	0.960	24.760	24.952	-0.77
1/8	19.743	9.000	0.988	34.958	34.268	1.97
$\phi=30^\circ$						
8	12.760	1.857	0.130	17.923	18.058	-0.75
4	12.782	1.982	0.236	18.013	18.077	-0.35
2	12.875	2.232	0.398	18.277	18.235	0.23
4/3	13.012	2.482	0.513	18.633	18.509	0.66
1	13.246	2.732	0.598	19.062	18.961	0.53
3/4	13.599	3.065	0.681	19.720	19.672	0.25
1/2	14.323	3.732	0.785	21.220	21.249	-0.14
1/4	16.284	5.732	0.909	26.178	26.295	-0.44
1/8	18.479	9.732	0.968	35.489	34.747	2.09

Table 6. TRAPEZOIDAL MICROCHANNELS DATA [7]

channel	b	a	h	ϵ	β	$fRe_{\sqrt{A}}$		
						model	data	%dif
	μm	μm	μm	—	—			
N1-100	100	20.1	56.4	1.06	0.56	13.85	14.48	-4.5
N1-150	150	70.1	56.4	1.95	0.87	15.61	15.95	-2.2
N1-200	200	120.2	56.4	2.84	0.94	18.34	18.74	-2.2
N1-500	500	420	56.5	8.14	0.99	33.38	31.55	5.5
N1-1000	1000	920	56.5	16.99	1.00	50.86	45.76	10.0
N1-4000	4000	3920	56.5	70.10	1.00	108.32	93.13	14.0
N2-50	50	0	35.3	0.71	0.00	13.50	13.95	-3.3
N2-100	100	39.9	42.4	1.65	0.82	14.83	14.91	-0.6
N2-150	150	89.9	42.4	2.83	0.94	18.29	18.22	0.4
N2-200	200	140	42.4	4.01	0.97	22.06	22.30	-1.1
N2-500	500	440	42.4	11.09	1.00	39.95	38.08	4.7
N2-1000	1000	940	42.4	22.89	1.00	59.94	54.60	8.9
N2-4000	4000	3940	42.4	93.70	1.00	125.76	110.70	12.0
N3-50	50	0	35.3	0.71	0.00	13.50	13.62	-0.9
N3-100	100	0	70.6	0.71	0.00	13.50	14.29	-5.8
N3-150	150	0	105.9	0.71	0.00	13.50	14.03	-3.9
N3-200	200	0	141.2	0.71	0.00	13.50	14.66	-8.6
N3-500	500	284	152.5	2.57	0.92	17.48	17.47	0.0
N3-1000	1000	784	152.5	5.85	0.99	27.46	26.45	3.7
N3-2000	2000	1784	152.5	12.40	1.00	42.59	39.57	7.1
N3-4000	4000	3784	152.5	25.52	1.00	63.57	57.07	10.2
N4-100	100	0	70.6	0.71	0.00	13.50	13.98	-3.5
N4-200	200	27.2	122.0	0.93	0.42	13.76	15.10	-9.7
N4-500	500	327	122.2	3.38	0.96	20.08	20.99	-4.5
N4-1000	1000	827	122.2	7.48	0.99	31.75	31.54	0.6
N4-4000	4000	3828	121.5	32.22	1.00	72.07	69.88	3.0
N5-150	150	47.4	72.5	1.36	0.73	14.24	14.87	-4.5
N6-500	500	279	156.1	2.50	0.92	17.24	17.07	1.0

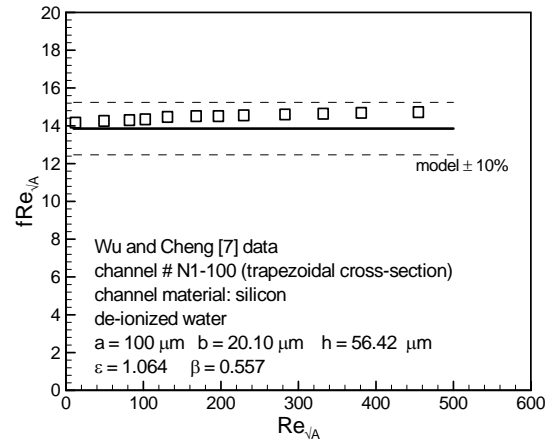


Figure 5. COMPARISON OF EXPERIMENTAL DATA [7] WITH MODEL

one $fRe_{\sqrt{A}}$ value can be obtained. Table 6 presents the predicted $fRe_{\sqrt{A}}$ values by the approximate model and the averaged values of the reported experimental values of $fRe_{\sqrt{A}}$ [7]. As shown, the agreement between the predicted values and the experimental values are good and within the experiment uncertainty. The channels considered by [7] cover a wide range of geometrical parameters, i.e., $0.71 \leq \epsilon \leq 97.70$ and $0 \leq \beta \leq 1$, as a result the data include triangular and

rectangular microchannels. It should be noted that, in spite of the different dimensions, channels N2-50, N3-50, N3-100, N3-150, N3-200, and N4-100 have the same values of β and ϵ ; thus they are geometrically equivalent. It is interesting to observe that the predicted and the measured $fRe_{\sqrt{A}}$ values are identical for these channels, as expected. Figure 7 illustrates the comparison between all trapezoidal data [7]

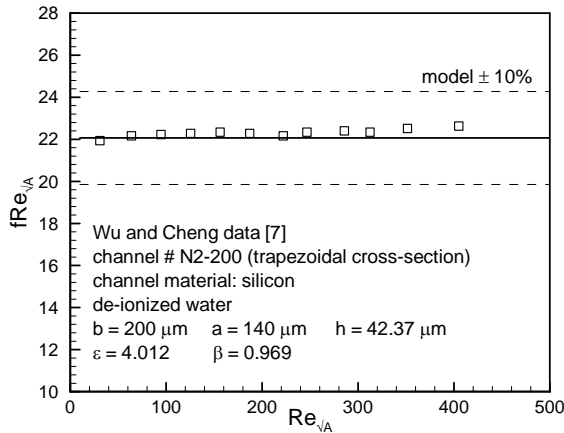


Figure 6. COMPARISON OF EXPERIMENTAL DATA [7] WITH MODEL

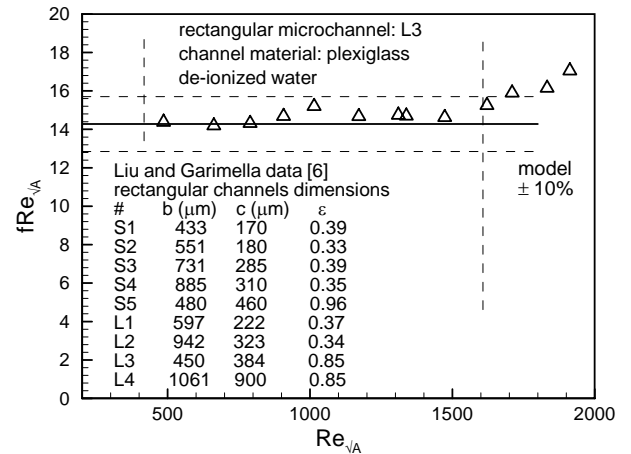


Figure 8. COMPARISON OF EXPERIMENTAL DATA [6] WITH MODEL

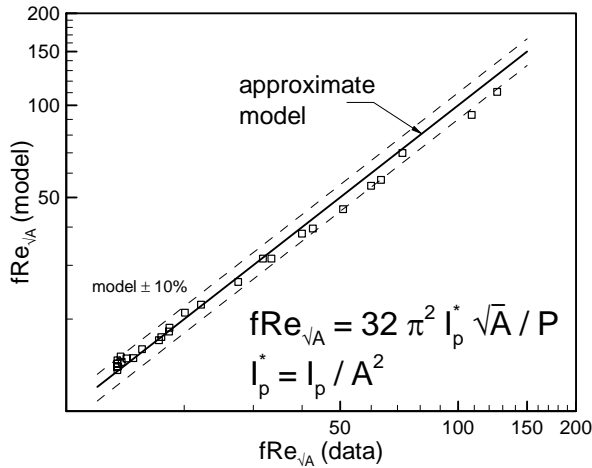


Figure 7. COMPARISON BETWEEN MODEL AND ALL TRAPEZOIDAL DATA [7]

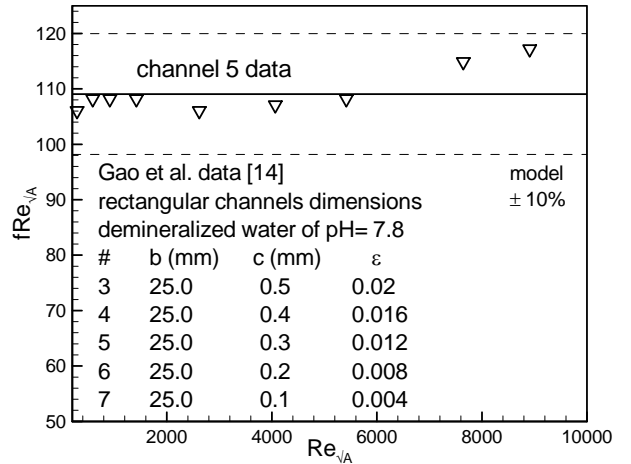


Figure 9. COMPARISON OF EXPERIMENTAL DATA [14] WITH MODEL

and the proposed model. The $\pm 10\%$ bounds are also shown in the plot, to better demonstrate the agreement between the data and the model.

Liu and Garimella [6] carried out experiments and measured the friction factor in rectangular microchannels. They did not observe any scale-related phenomena in their experiments and concluded that the conventional theory can be used to predict the flow behavior in microchannels in the range of dimensions considered. They [6] measured and reported the relative surface roughness of the channels to be negligible, thus their channels can be considered smooth (see Fig. 8 for channels dimensions). Figure 8 also shows the comparison between the model and the channel L3 of

data [6].

Gao et al. [14] experimentally investigated laminar fully developed flow in rectangular microchannels. They designed their experiments to be able to change the height of the channels tested while the width remained constant at 25 mm. They conducted several experiments with several channel heights, see Fig. 9 for the channels dimensions used in this study. Gao et al. [14] measured the roughness of the channel and reported negligible relative roughness, thus their channels can be considered smooth. Figure 9 shows the comparison of the model and data [14].

Following the same method described for trapezoidal data, the reported values of $fRe_{\sqrt{A}}$ for rectangular microchannels are averaged and plotted against both approxi-

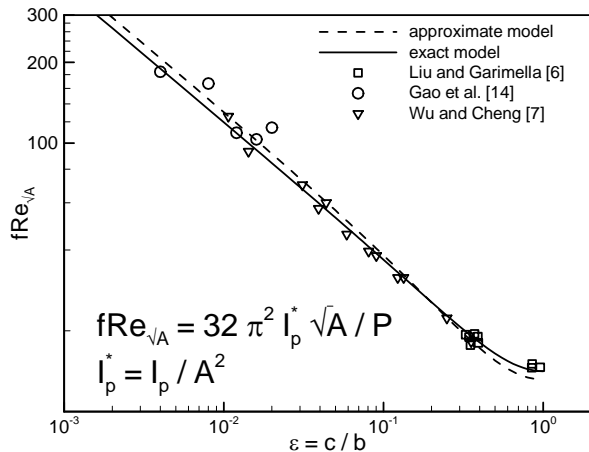


Figure 10. COMPARISON BETWEEN MODEL AND ALL RECTANGULAR DATA [6,7,14]

mate and exact models in Fig. 10. As previously discussed, the maximum difference between the exact and approximate solutions for the rectangular channel is less than 8%. As shown in Fig. 10, the collected data cover a wide range of the aspect ratio $\epsilon = c/b$, almost three decades; also the relative difference between the data and model is within the accuracy of the experiments.

6 SUMMARY AND CONCLUSIONS

Pressure drop of fully developed laminar flow in smooth arbitrary cross-sections channels is studied. Using existing analytical solutions for fluid flow, relationships are derived for $fRe_{\sqrt{A}}$ for selected cross-sections. It is observed through analysis that the square root of area \sqrt{A} , as the characteristic length scale, is superior to the conventional hydraulic diameter, D_h . Thus it is recommended to use \sqrt{A} instead of D_h .

A compact approximate model is proposed that predicts the pressure drop of fully developed, laminar flow in channels of arbitrary cross-section. The model is only a function of geometrical parameters of the cross-section, i.e., area, perimeter, and polar moment of inertia. The proposed model is compared with analytical and numerical solutions for several shapes. Except for the equilateral triangular channel (with 14% difference), the present model successfully predicts the pressure drop for a wide variety of shapes with a maximum difference on the order of 8%. Moreover, a compact model is developed using a mapping approach, which predicts the $fRe_{\sqrt{A}}$ for isosceles triangular channels with a maximum difference less than 3.5%

The proposed model is also validated with either ex-

perimental data or exact analytical solutions for rectangular, trapezoidal, triangular (isosceles), square, and circular cross-sections collected by several researchers and shows good agreement.

ACKNOWLEDGMENT

The authors gratefully acknowledge the financial support of the Centre for Microelectronics Assembly and Packaging, CMAP and the Natural Sciences and Engineering Research Council of Canada, NSERC.

REFERENCES

- [1] C. Yang, J. Wu, H. Chien, and S. Lu, "Friction characteristics of water, r-134a, and air in small tubes," *Microscale Thermophysical Engineering*, vol. 7, pp. 335–348, 2003.
- [2] G. L. Morini, "Laminar-to-turbulent flow transition in microchannels," *Microscale Thermophysical Engineering*, vol. 8, pp. 15–30, 2004.
- [3] D. B. Tuckerman and R. F. Pease, "High-performance heat sinking for vlsi," *IEEE Electronic Device Letters*, no. 5, pp. 126–129, 1981.
- [4] D. Pfund, D. Rector, A. Shekarriz, A. Popescu, and J. Welty, "Pressure drop measurements in a microchannel," *AIChE Journal*, vol. 46, no. 8, pp. 1496–1507, 2000.
- [5] M. Bahrami, M. M. Yovanovich, and J. R. Culham, "Pressure drop of fully developed, laminar flow in rough microtubes," *To be presented in ASME 3rd International Conference on Microchannels*, July 13-15, U. of Toronto, Canada, 2005.
- [6] D. Liu and S. Garimella, "Investigation of liquid flow in microchannels," *Journal of Thermophysics and Heat Transfer*, AIAA, vol. 18, no. 1, pp. 65–72, 2004.
- [7] H. Y. Wu and P. Cheng, "Friction factors in smooth trapezoidal silicon microchannels with different aspect ratios," *International Journal of Heat and Mass Transfer*, vol. 46, pp. 2519–2525, 2003.
- [8] R. K. Shah and A. L. London, *Laminar Flow Forced Convection In Ducts*. New York: Academic Press, 1978.
- [9] F. M. White, *Viscous Fluid Flow*, ch. 3. New York: McGraw-Hill, Inc., 1974.
- [10] M. M. Yovanovich, *Advanced Heat Conduction*, ch. 12. In Preparation.
- [11] Y. S. Muzychka and M. M. Yovanovich, "Modeling friction factors in non-circular ducts for developing laminar flow," *2nd AIAA Theoretical Fluid Mechanics Meeting*, June 15-18, Albuquerque, NM, 1998.
- [12] Y. S. Muzychka and M. M. Yovanovich, "Laminar flow

friction and heat transfer in non-circular ducts and channels part 1: Hydrodynamic problem,” *Proceedings of Compact Heat Exchangers, A Festschrift on the 60th Birthday of Ramesh K. Shah, Grenoble, France*, pp. 123–130, 2002.

- [13] S. P. Timoshenko and J. N. Goodier, *Theory of Elasticity*, ch. 10. New York: McGraw-Hill, Inc., 1970.
- [14] P. Gao, S. L. Person, and M. Favre-Marinet, “Scale effects on hydrodynamics and heat transfer in two-dimensional mini and microchannels,” *International Journal of Thermal Sciences*, vol. 41, pp. 1017–1027, 2002.
- [15] S. W. Churchill and R. Usagi, “A general expression for the correlation of rates of transfer and other phenomena,” *American Institute of Chemical Engineers*, vol. 18, pp. 1121–1128, 1972.

A ISOSCELES TRIANGULAR CHANNELS

To calculate the pressure drop in isosceles triangular channels, a *mapping approach* is used. Shah and London [8] reported numerical values of fRe_{D_h} for isosceles triangular channels as a function of the aspect ratio defined as α^*

$$\alpha^* = \frac{h}{b} \quad (46)$$

The reported numerical values [8] were converted to $fRe_{\sqrt{A}}$. Plotting $fRe_{\sqrt{A}}$ versus α^* reveals that the solution has two asymptotes corresponding to the angle ϕ as it approaches 0 and 180° as shown in Fig. 11. It is interesting to observe that these two asymptotes are both similar to very narrow rectangular channels. Thus Eq. (19) can be used to predict $fRe_{\sqrt{A}}$ in both limits. Equation (19) can be written in terms of α^* , defined by [8], as follows:

$$fRe_{\sqrt{A}} = \begin{cases} \frac{12}{\sqrt{2\alpha^*}} & \alpha^* \rightarrow 0 \\ \frac{12\sqrt{\alpha^*}}{\sqrt{2}} & \alpha^* \rightarrow \infty \end{cases} \quad (47)$$

To find relationships between α^* of triangular channel and ϵ of equivalent rectangular channel, the cross-sectional area of the equivalent rectangular is set equal to the triangular channel, see Fig. 11. Using the blending technique of Churchill and Usagi [15], a compact correlation can be developed by combining the above asymptotes as follows:

$$fRe_{\sqrt{A}} = 6 \left[\left(\frac{2}{\alpha^*} \right)^{n/2} + (2\alpha^*)^{n/2} \right]^{1/n} \quad (48)$$

The value of the *fitting* parameter n can be obtained by comparing the compact correlation with the numerical values for α^* in the range [0.5, 2]. If we choose $\alpha^* = 1$, then

$fRe_{\sqrt{A}} = 15.24$, and the value of $n = 1.184$ gives excellent agreement at this point. If we select $n = 1.20$, the maximum difference of about 3.5% occurs at $\alpha^* = 0.3$. For the equilateral triangle where $\alpha^* = \sqrt{3}/2$, the compact model with $n = 1.20$, gives $fRe_{\sqrt{A}} = 15.24$ which is about 0.3% greater than the numerical value of 15.19. Figure 12 presents the

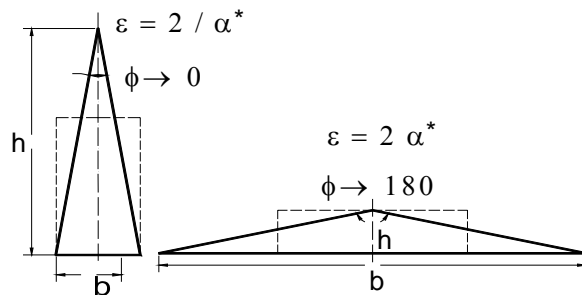


Figure 11. TWO LIMITS OF ISOSCELES TRIANGULAR CHANNEL

numerical values of $fRe_{\sqrt{A}}$ reported by [8], the two asymptotes, and the compact model, Eq. (48), with $n = 1.20$.

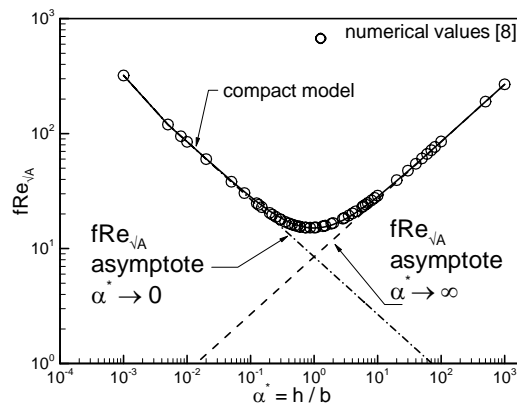
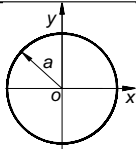
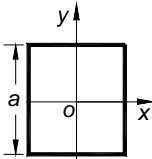
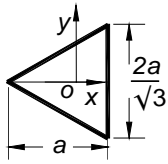
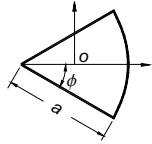
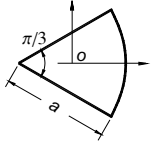
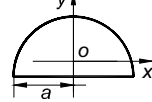
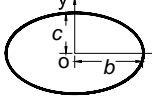
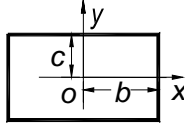


Figure 12. $fRe_{\sqrt{A}}$ FOR ISOSCELES TRIANGULAR CHANNELS

Table 2. GEOMETRIC PARAMETER AND APPROXIMATE MODEL FOR VARIOUS CROSS SECTIONS

cross-section	I_p^*	\sqrt{A}/P	$f Re_{\sqrt{A}}$	
			$32\pi^2 I_p^* \sqrt{A}/P$	exact
	$\frac{1}{2\pi}$	$\frac{1}{2\sqrt{\pi}}$	14.18	14.18
	$\frac{1}{6}$	$\frac{1}{4}$	13.16	14.13
	$\frac{\sqrt{3}}{9}$	$\frac{\sqrt{3}}{6(3)^{1/4}}$	13.33	15.19
	$\frac{9\phi^2 - 8\sin^2\phi}{18\phi^3}$	$\frac{\sqrt{\phi}}{2(1+\phi)}$	$\frac{(9\phi^2 - 8\sin^2\phi)\sqrt{\phi}}{36\phi^3(1+\phi)}$	$\frac{\phi\sqrt{\phi}}{(1+\phi)g(\phi)^{[*]}}$
	circular sector	$\phi = \frac{\pi}{6}$	13.57	14.92
	semi-circle	$\phi = \frac{\pi}{2}$	15.67	16.17
	$\frac{1+\epsilon^2}{4\pi\epsilon}$	$\frac{\sqrt{\pi\epsilon}}{4E(\sqrt{1-\epsilon^2})}$	$\frac{2\pi\sqrt{\pi}(1+\epsilon^2)}{\sqrt{\epsilon}E(\sqrt{1-\epsilon^2})}$	$\frac{2\pi\sqrt{\pi}(1+\epsilon^2)}{\sqrt{\epsilon}E(\sqrt{1-\epsilon^2})}$
	$\frac{1+\epsilon^2}{12\epsilon}$	$\frac{\sqrt{\epsilon}}{2(1+\epsilon)}$	$\frac{4\pi^2(1+\epsilon^2)}{3\sqrt{\epsilon}(1+\epsilon)}$	$\frac{12}{\left[1 - \frac{192}{\pi^5}\epsilon \tanh\left(\frac{\pi}{2\epsilon}\right)\right](1+\epsilon)\sqrt{\epsilon}}$

$\epsilon = c/b$

[*] see Table 1